Applied Catalysis B: Environmental 217 (2017) 485–493

Contents lists available at ScienceDirect

Applied Catalysis B: Environmental

journal homepage: www.elsevier.com/locate/apcatb

Cu_2O/TiO_2 heterostructures for CO_2 reduction through a direct Z-scheme: Protecting Cu_2O from photocorrosion

Matías E. Aguirre[a], Ruixin Zhou[b], Alexis J. Eugene[b], Marcelo I. Guzman[b,*], María A. Grela[a,*]

[a] Instituto de Investigaciones Físicas de Mar del Plata (IFIMAR)-Departamento de Química, Facultad de Ciencias Exactas y Naturales, Universidad Nacional de Mar del Plata-CONICET, Funes 3350, 7600, Mar del Plata, Prov. de Buenos Aires, Argentina
[b] Department of Chemistry, University of Kentucky, Lexington, KY 40506, USA

ARTICLE INFO

Article history:
Received 6 March 2017
Received in revised form 8 May 2017
Accepted 20 May 2017
Available online 22 May 2017

Keywords:
CO_2 reduction
Cu_2O/TiO_2 composite photocatalyst
Z-scheme
Cu_2O photocorrosion

ABSTRACT

The development of artificial photosynthesis aims to solve the increasing energy demand and associated environmental problems. A model photosynthetic system employing a composite of semiconductors with a Z-scheme can potentially mimic the combined power of photosystems 1 and 2 to transfer electrons. In this work, octahedral cuprous oxide covered with titanium dioxide nanoparticles (Cu_2O/TiO_2) are synthesized by a solvothermal strategy that provides high morphological and crystallographic control. The formation of a *p-n* heterojunction and characterization of the Type II band alignment of the composite are performed by diffuse reflectance UV-visible (DRUV) spectroscopy, ultraviolet photoelectron spectroscopy (UPS), and X-ray photoelectron spectroscopy (XPS). Upon UV-visible irradiation ($\lambda \geq 305$ nm) of the composite in the presence of water vapor as the hole scavenger, the photoreduction of CO_2(g) proceeds selectively to generate CO(g). The production rate of CO by the composite, $R_{CO} = 2.11\ \mu mol\ g_{cat}^{-1}\ h^{-1}$, is 4-times larger than for pure Cu_2O under identical conditions. Contrasting XPS analyses of Cu_2O and Cu_2O/TiO_2, during photocatalysts operation and the detection of photogenerated hydroxyl radicals ($HO^{\bullet}$) in the heterostructure at variance with the results obtained for pure Cu_2O are taken as evidences that TiO_2 protects Cu_2O from undergoing photocorrosion. These results provide direct evidence of an efficient Z-scheme as the main mechanism for harvesting energy during CO_2 reduction in the synthesized materials.

1. Introduction

The design of efficient photocatalysts aimed at the conversion of CO_2 to useful chemicals is a scientific challenge which is driven by the shortage of energy resources and the increased concentration of this greenhouse gas in the atmosphere [1–4]. The high stability of the linear CO_2 molecule makes its reduction difficult and usually demands scarce and expensive species, such as ruthenium or rhenium complexes [4–7]. The use of heterogeneous photocatalytic systems involving TiO_2, ZnO, or ZnS provide a possible, although less efficient alternative for carbon dioxide reduction under UV excitation [8–10]. It should be noticed that none of these semiconductors provides sufficient potential to mediate the one electron reduction of CO_2 (Equation (1)), since their conduction bands lie below the homogeneous reduction potential of carbon dioxide, $E^{\bullet}(CO_2/CO_2^{\bullet -}) = -1.9$ V [11].

$$CO_2 + e^- \rightarrow CO_2^{\bullet -} \quad (1)$$

Although adsorption on semiconductor surfaces would certainly bend the linear CO_2 molecule and lower the energy demand for reaction 1, the considerable gap between the CO_2 LUMO and the conduction band (CB) probably prevents direct CO_2 reduction by CB electrons [12]. Thus, the photocatalytic reduction of CO_2 frequently involves the use of sacrificial donors (*i.e.*, alcohols) that generate reactive intermediates (hydroxyalkyl radicals) which can accomplish reaction (1). It is also apparent that the low photon intermittency usually employed under practical photocatalytic experiments is against the occurrence of multielectronic processes [13], which could by-pass the high energy intermediate $CO_2^{\bullet -}$ [14].

Cuprous oxide (Cu_2O) is an interesting *p*-semiconductor whose conduction band is much more energetic than the commonly used wide bandgap semiconductors. The bandgap of cuprous oxide is $E_{gap,2} \approx 2$-2.2 eV, while its conduction band is poised at

* Corresponding authors.
E-mail addresses: marcelo.guzman@uky.edu (M.I. Guzman), magrela@mdp.edu.ar (M.A. Grela).

http://dx.doi.org/10.1016/j.apcatb.2017.05.058
0926-3373/

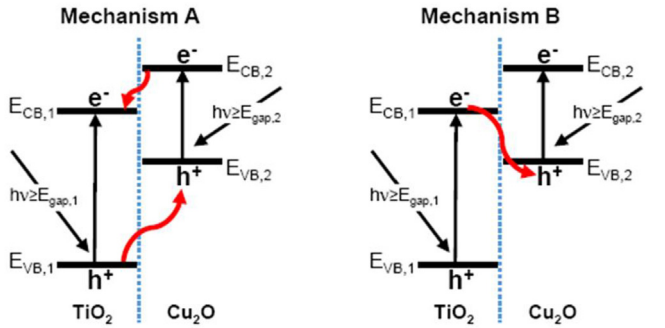

Scheme 1. Schematic representation of the processes that can take place in a system consisting of two semiconductors in electrical contact under irradiation with photons of suitable energy. (A) Double-charge transfer, and (B) direct Z-scheme mechanism.

$E_{CB,2} = -1.4$ eV vs NHE at pH = 7 [15]. Unfortunately, as commonly found for semiconductors active in the visible region its photostability is scarce [16]. However, it can be envisaged that surface modification of Cu_2O with a *n*-type wide bandgap semiconductor such as TiO_2 could generate a Type II heterostructure and avoid Cu_2O photocorrosion as discussed below.

Scheme 1 shows the expected energy diagram for the Type II Cu_2O/TiO_2 heterostructure [17].

Simultaneous excitation of the individual components of the composite leads to an electron-hole pair in each photocatalytic center. Different mechanisms can be envisaged to rationalize the charge transfer across the interface in *p-n* heterojunctions. Scheme 1A represents a double-charge transfer mechanism, in which the Cu_2O electrons move to the TiO_2 center and TiO_2 holes migrate to Cu_2O [18,19]. Alternatively, Scheme 1B involves a direct Z-scheme mechanism [20–23] where the TiO_2 electrons are used to scavenge Cu_2O holes. The double-charge transfer mechanism favors charge separation, at the expense of a decrease in the potential energy of electrons and holes. Moreover, it generates an excess of holes in Cu_2O that could lead to its photocorrosion in absence of a suitable electron donor. Instead, under the Z-scheme mechanism the electron transfer across the interface could provide a way for preserving Cu_2O photostability while maintaining a high reduction potential. Both, mechanisms A and B (Scheme 1), have been previously invoked to explain the higher efficiency of the heterostructures in comparison to the individual counterparts; however, the factors favoring one of the two mechanisms remain elusive.

In this work, we synthesize and fully characterize a type II heterostructure based on *p*-type octahedral Cu_2O and *n*-type TiO_2 nanoparticles. The synthetized material shows an enhanced efficiency for CO_2 photoreduction in comparison to the individual materials. Based on comparative X-ray photoelectron spectroscopy (XPS) studies of Cu_2O and Cu_2O/TiO_2 heterostructures under UV-visible irradiation, we provide direct experimental evidence in favor of the Z-scheme mechanism.

2. Experimental

2.1. Chemicals and materials

Copper(II) chloride dihydrate ($CuCl_2{\cdot}2H_2O$, 99.4% assay, J. T. Baker), polyvinylpyrrolidone (PVP, average MW ≈ 29000 from Aldrich), sodium hydroxide (NaOH, 99.3% assay, VWR), L-ascorbic acid (99.7% assay, Sigma-Aldrich), ethanol (absolute for analysis, 99.9% assay, EMD Chemicals) and titanium(IV) butoxide (97.0% assay, Sigma-Aldrich) were used as received. Carbon dioxide (CO_2, UHP) and carbon monoxide (CO, CP) were purchased from Scott Gross. All procedures employed ultrapure water (18.2 MΩ cm, ELGA PURELAB flex, Veolia).

2.2. Synthesis of Cu_2O octahedra

Cu_2O synthesis closely follows a previous published procedure [24]. In a typical experiment, 6.66 g of PVP were dissolved in an aqueous solution of $CuCl_2{\cdot}2H_2O$ (0.01 mol L^{-1}, 100 mL) at 55 °C. Then, 10.0 mL NaOH aqueous solution (2.0 mol L^{-1}) was added dropwise into the above transparent light green solution. During this process, the solution color changes from blue-green to dark brown. The reaction mixture was stirred for 0.5 h, keeping the temperature at 55 °C. Afterwards, 10 mL of an aqueous ascorbic acid solution (0.6 mol L^{-1}) was added dropwise and the mixture was aged for 3 h under constant stirring and strict temperature control (55 °C). This last stage gradually produces a red suspension. The resulting precipitate was collected by centrifugation and washed consecutively with 10 mL of deionized water and absolute ethanol (5 times). Finally, the solid was dried under vacuum at 60 °C for 5 h for further use and characterization.

When mentioned a thermal treatment was applied to the as-synthesized solid. Briefly, the solid was resuspended in absolute ethanol, transferred to 200 mL Teflon-lined stainless steel autoclave and heated at 180 °C for 12 h in a programmable oven. An initial ramp of 1 °C min^{-1} was used to achieve the final temperature.

2.3. Preparation of TiO_2/Cu_2O

The modification of Cu_2O octahedral was performed following the procedure developed by Liu et al. [25]. Briefly, 186 mg of Cu_2O were resuspended in 65 mL of absolute ethanol with the aid of ultrasonication for 30 min, and the suspension was cooled at 0 °C. At this temperature, 1.3 mL of titanium (IV) butoxide ethanolic solution (0.1 mol L^{-1}) were added dropwise into the Cu_2O suspension and stirred for 1 h at 0 °C. Afterwards, 6.5 mL of a water:ethanol solution (volume ratio 1:4) were added dropwise to the mixture under vigorous stirring for another hour. The reaction mixture was diluted with 98 mL of absolute ethanol, transferred to 200 mL Teflon-lined stainless steel autoclave and heated at 180 °C for 12 h in a programmable oven. An initial ramp of 1 °C min^{-1} was used to achieve the final temperature. The amount of Cu_2O and TiO_2 precursors used in this approach guarantee a nominal proportion of 0.05:0.95 of TiO_2:Cu_2O in weight. The product was collected by centrifugation and washed consecutively with 10 mL of deionized water and absolute ethanol (5 times). Finally, the solid was dried in vacuum at 60 °C for 5 h for further use and characterization.

Pure TiO_2 was obtained using the same solvothermal procedure described above, in absence of Cu_2O crystals.

2.4. Catalyst characterization

The crystalline properties of the as-prepared samples were analyzed via powder X-ray diffraction (XRD). The analysis was carried out on a X'Pert PRO (PANalytical) powder X-ray diffractometer, with Cu K_α (1.54 Å) as the incident radiation and operated at an accelerating voltage of 40 kV with a current intensity of 40 mA.

The morphology of the samples was observed by scanning electron microscopy (SEM) using a Hitachi S-4300 instrument with an accelerating voltage of 25 kV. A *ca.* 10 μL drop of colloidal suspension in ethanol (10 mg mL^{-1}) was put on a SEM grid and dried under a red light lamp. The phase distribution in the Au-metallized samples, was analyzed by Energy-Dispersive X-ray Spectroscopy (EDS) using a Jeol JSM-6460LV scanning electron microscope, operating at 15 kV coupled to a EDS probe Genesis XM4-Sys 60. X-ray photoelectron spectroscopy (XPS) measurements of the powdered samples were conducted using a PHI VersaProbe II spectrometer with an Al

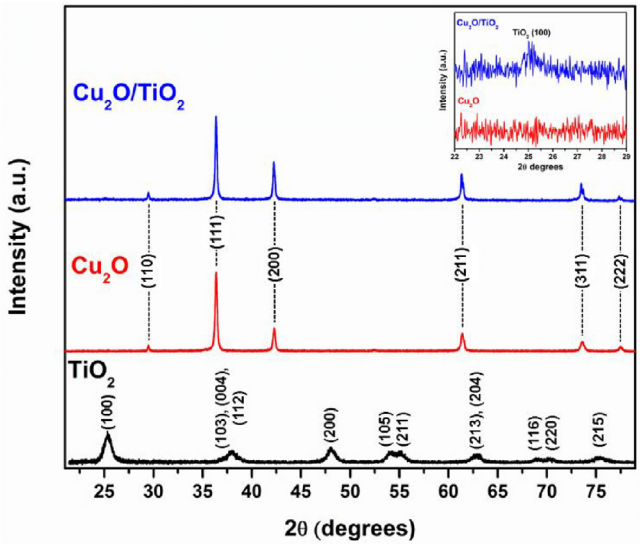

Fig. 1. X- ray diffraction patterns of (blue) Cu_2O/TiO_2, (red) Cu_2O and (black) TiO_2. The crystal planes from JCPDS are shown between parentheses. Inset shows an enlarged view of the region between θ = 22–29° of (blue) Cu_2O/TiO_2 and (red) Cu_2O diffractograms. (For interpretation of the references to colour in this figure legend, the reader is referred to the web version of this article.)

K-α anode (1486.6 eV photon energy, 86.6 W). Ultraviolet photoelectron spectroscopy (UPS) studies were carried out by using a PHI 5600 system with He (10.2 eV) as monochromatic light source with a polarization potential (bias) of −5.0 eV. All values determined from UPS analysis are referred to vacuum. The diffuse reflectance UV-visible (DRUV) spectra of the powered samples were obtained with an Evolution 220, ISA-220 accessory, Thermo Scientific UV−vis spectrophotometer using a built-in 10 mm silicon photodiode with a 60 mm Spectralon sphere. The ISA-220 accessory was used in a configuration to register the diffuse reflectance spectrum of dry solid powders as a Kubelka−Munk function against the certified Spectralon standard [14].

2.5. Photocatalytic studies

The photocatalytic experiments were performed in a 135 cm^3 customized quartz photoreactor with flat circular windows (diameter = 5.08 cm). Based on the elemental distribution obtained by SEM-EDS analysis (see Supporting Information, S1), 3 mL of suspensions of appropriate concentrations to deposit 30 mg of Cu_2O/TiO_2, 28.4 mg of Cu_2O, or 1.6 mg TiO_2 were uniformly deposited in one of the reactor windows, and left to dry overnight. The reactor was then filled with 1 atm CO_2(g) saturated with water vapor by sparging the gas during 20 min (0.5 L min^{-1}) through a gas wash bottle. The reactor sealed with septa was kept in the dark for 1 h before irradiation to ensure a homogenous internal atmosphere. UV-visible irradiation was performed with a collimated 1 kW high-pressure Hg (Xe) arc lamp provided with a water filter and a cut-off filter at $\lambda \geq 305$ nm (Newport) previously described [14]. The irradiance of the lamp was measured in the interval $305 \leq \lambda \leq 665$ nm with a calibrated radiometer (Ocean Optics). Gas aliquots of 0.5 cm^3 were taken from the reactor at different irradiation times for analysis by gas chromatography (SRI 8610C, Multiple Gas #3 GC) equipped with two columns (a silica gel HaySep D as column 1 and a MoleSieve 13X as column 2), a thermal conductivity detector (TCD), and a flame ionization (FID) detector interfaced to a methanizer. The irradiation of the photocatalyst and quantification of produced CO(g) were performed at room temperature (20 °C). Additionally, the reaction products were identified by FTIR spectroscopy using a 2.4 m path length infrared gas cell with ZnSe windows (PIKE) thermostatted at 100 °C mounted in an iZ10 FTIR module connected to an infrared microscope (Thermo Scientific Nicolet iN10) [26]. Furthermore, photocatalyst alteration during irradiation was monitored by XPS using a Thermo-Scientific K-Alpha X-ray Photoelectron Spectrometer with an Al K-α anode (1486.6 eV photon energy, 300 W).

The formation of hydroxyl radicals ($HO^{\bullet}$) on the surface of irradiated Cu_2O/TiO_2 was quantified using the coumarin fluorescence method with a Lumina Fluorescence Spectrometer (Thermo Scientific) using excitation at λ_{exc} = 332 nm. While coumarin is a poorly fluorescent molecule, it is an excellent probe to quantify [$HO^{\bullet}$] trapped in the produced 7-hydroxycoumarin. 7-Hydroxycoumarin has a characteristic fluorescent signal at λ_{em} = 456 nm [27], which is proportional to the formed [$HO^{\bullet}$] [28]. The experimental procedure followed the same steps of the photoreduction experiments, except that 30 mg of coumarin (Alfa Aesar, 98.0%) were deposited on top of the 30 mg of nanocomposite thin film for a 1:1 mass ratio [20]. Each data point corresponds to individual irradiation experiments at times of 0, 1, 2, and 3 h. Controls in the dark and with the individual components were also performed. Samples were extracted with 51 mL of water [20], centrifuged at 4400 rpm for 5 min, and forced through a filter (Acrodisc 0.2 μm pore size; Pall Corp.) to quantify by standard addition the 7-hydroxycoumarin (Acros, 98.5%) produced.

3. Results and discussion

3.1. Selection of Cu_2O shape and composite architecture

By modifying the reaction conditions, *i.e.*, the relative amount between the capping agent and Cu_2O precursors, the shape of Cu_2O crystals can be easily modified from cubic to octahedra. This issue has attracted the attention of many researchers, who concluded that octahedral Cu_2O with exposed (111) facets exhibited much higher photocatalytic activity than the cubic structure [29–31]. It is apparent that crystalline (111) facets containing active Cu atoms can increase the interaction with donors and acceptors [24,32]. Guided by these conditions, we choose Cu_2O octahedral as the starting point to design the composite [33,34]. Also, since the hybrid composite would allow free access of the acceptor and donor to both surfaces, we regulated the concentration of the semiconductors precursors taking into account the individual size and surface area in order to warrant nearly all of TiO_2 nanoparticles cover the surface of Cu_2O and the amount of free TiO_2 nanoparticles is depreciable as verified by SEM analysis. The actual proportion by weight in the composite was estimated by SEM-EDS analysis to be 0.053:0.947 of TiO_2:Cu_2O, in very good agreement with the nominal proportion (See Fig. S1).

3.2. XRD and SEM analysis of crystal structure and morphology

Fig. 1 shows the X-ray diffraction patterns of the synthesized Cu_2O octahedra, TiO_2 and Cu_2O/TiO_2. For both Cu_2O and Cu_2O/TiO_2, all the peaks belong to the face-centered cubic Cu_2O phase (PDF Card No. 05-0667) and no diffraction peaks of CuO or metallic Cu could be detected. The strong and sharp peaks attributable to Cu_2O indicate a high degree of crystallinity. A low-intensity diffraction peak at θ = 25.08 is present in the Cu_2O/TiO_2 diffraction pattern, and ascribed to the (100) plane of anatase, as shown in the inset of Fig. 1.

The XRD pattern of pure TiO_2 (Fig. 1), obtained in a parallel synthesis is in agreement with the report for anatase (JCPDS 21–1272).

SEM measurements, Fig. 2(a, b), show that after solvothermal treatment of the titanium(IV) butoxide ethanolic solution in the presence of Cu_2O octahedral particles, fine TiO_2 nanoparticles cover Cu_2O (Fig. 2(c, d)). It is also apparent that Cu_2O morphology is not

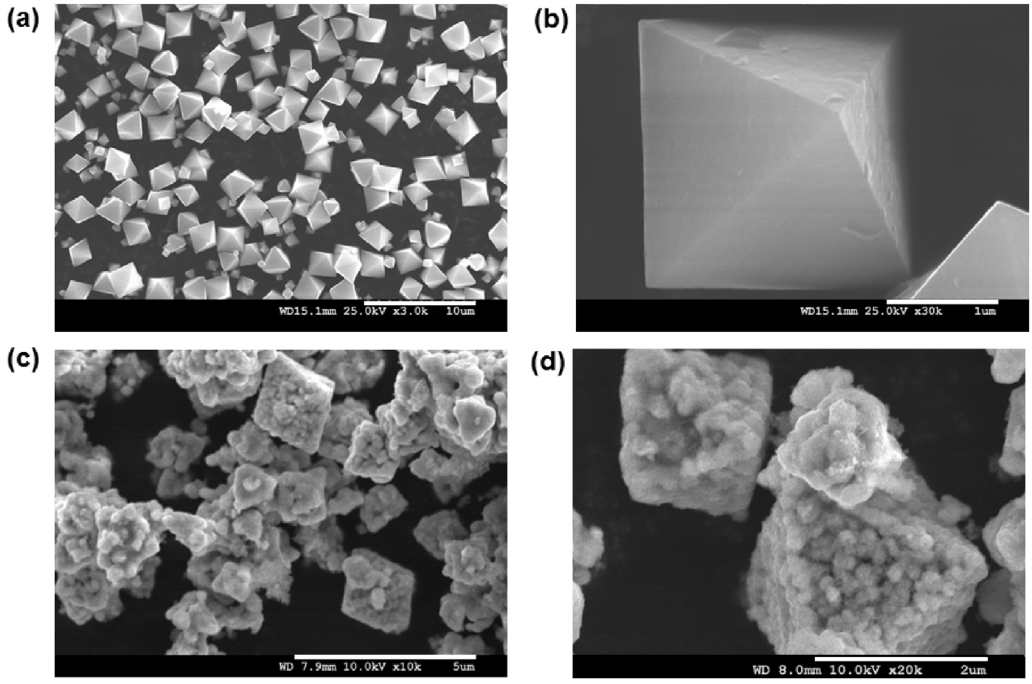

Fig. 2. SEM images for (a, b) Cu_2O, (c, d) Cu_2O/TiO_2. The left hand side panels show images obtained with low magnification, while the aspect of isolated particles obtained with high magnification are shown at the right hand side.

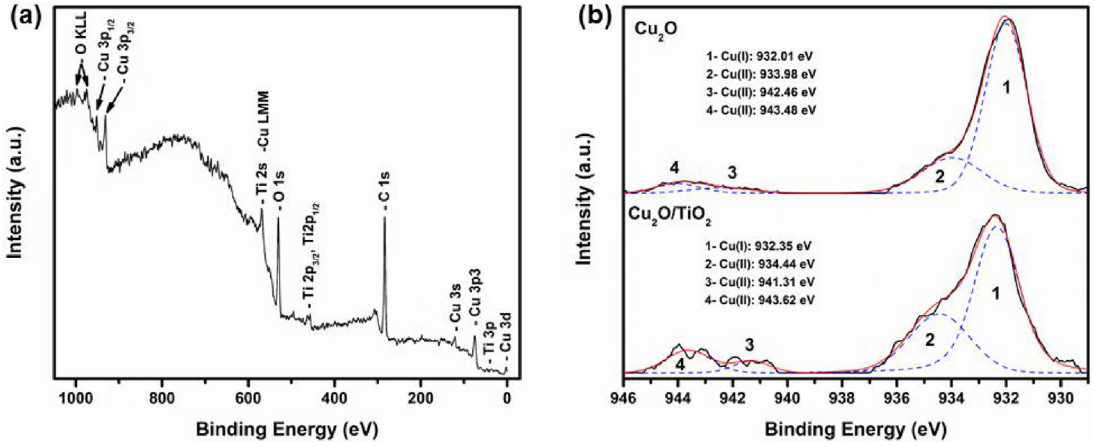

Fig. 3. (a) XPS survey spectrum for Cu_2O/TiO_2 composite. (b) high resolution spectra for $Cu2p_{3/2}$ (peak 1) and shake-up satellite peaks (2, 3, and 4) in Cu_2O (top) and Cu_2O/TiO_2 (bottom) are shown as black solid lines. For comparison, the deconvoluted components (blue dash line) and the total fit from the sum of the components (red solid line) are also shown. See text for details. (For interpretation of the references to colour in this figure legend, the reader is referred to the web version of this article.)

altered by the thermal treatment, thus, the difference observed in the photocatalytic activity of the composite presented below cannot be attributed to changes in the surface chemistry of Cu_2O particles, but rather to the presence of TiO_2. Distribution phase was confirmed by EDS (Fig. S1).

3.3. Surface characterization by XPS analysis

Fig. 3a shows the XPS survey spectrum for Cu_2O/TiO_2 composites, which demonstrates the existence of Cu, Ti and O in the sample. The C 1s peak, associated to the widespread presence of carbon in the environment is also clearly observed. Fig. 3b compares the high resolution XPS spectrum in the region of Cu $2p_{3/2}$ for pure Cu_2O and Cu_2O/TiO_2 composite. The same deconvolution procedure was applied throughout the analysis of the peaks and basically involves the subtraction of a Shirley-type baseline and the use of Voigt-type functions to reproduce the spectra. For Cu_2O the main peak is centered at 932.01 eV and is readily assigned to Cu(I) [35], while the shake-up satellite peaks with higher binding energy (933.98, 942.46, 943.98 eV) confirm the presence of an unfilled Cu 3d shell corresponding to Cu(II) species at the Cu_2O surface. This observation has been commonly attributed to the oxidation of Cu(I) during sample preparation for analysis [36]. For the Cu_2O/TiO_2 composites, the position of the peaks is similar (See Fig. 3b) but the relative area Cu(I):Cu(II) obtained through the deconvolution of Cu $2p_{3/2}$ spectrum changes from 0.75:0.25 (for pure Cu_2O) to 0.65:0.35 (in Cu_2O/TiO_2 composites). The previous information together with the results from XRD diffractograms suggests that a minimum fraction of surface copper changes its electronic state during the solvothermal treatment.

The high resolution XPS spectrum of Ti 2p in Cu_2O/TiO_2 can be adjusted with great accuracy with two Voigt-type functions centered in 458.31 and 464.19 eV that can be assigned to Ti $2p_{3/2}$ and Ti $2p_{1/2}$, respectively for Ti(IV) [37] in agreement with the results

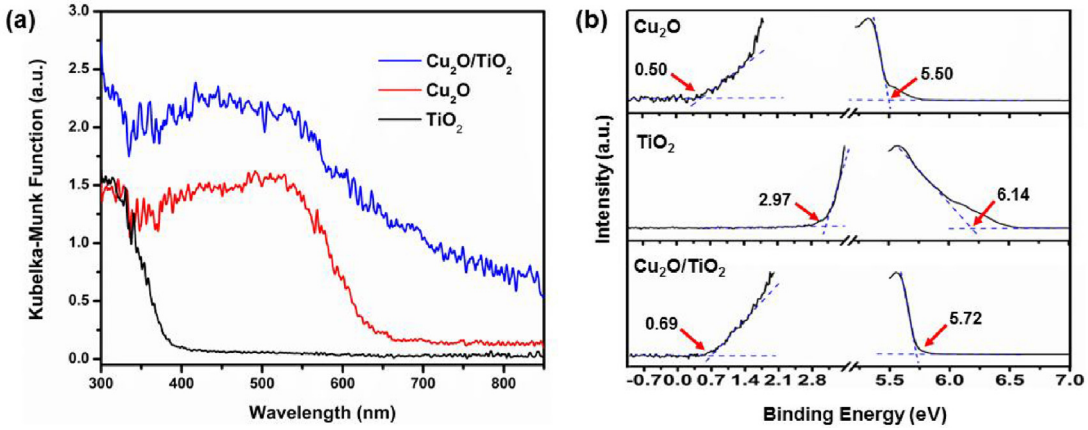

Fig. 4. (a) UV-visible absorption spectra for solid samples. (b) UPS spectra for Cu_2O octahedral (top), pure TiO_2 (center), and Cu_2O/TiO_2 heterostructure (bottom). Extrapolations to the left and right hand sides correspond to the onset values for the valence band and secondary electron spectra, respectively. A complete description is available in the Supporting Information (see Fig. S5).

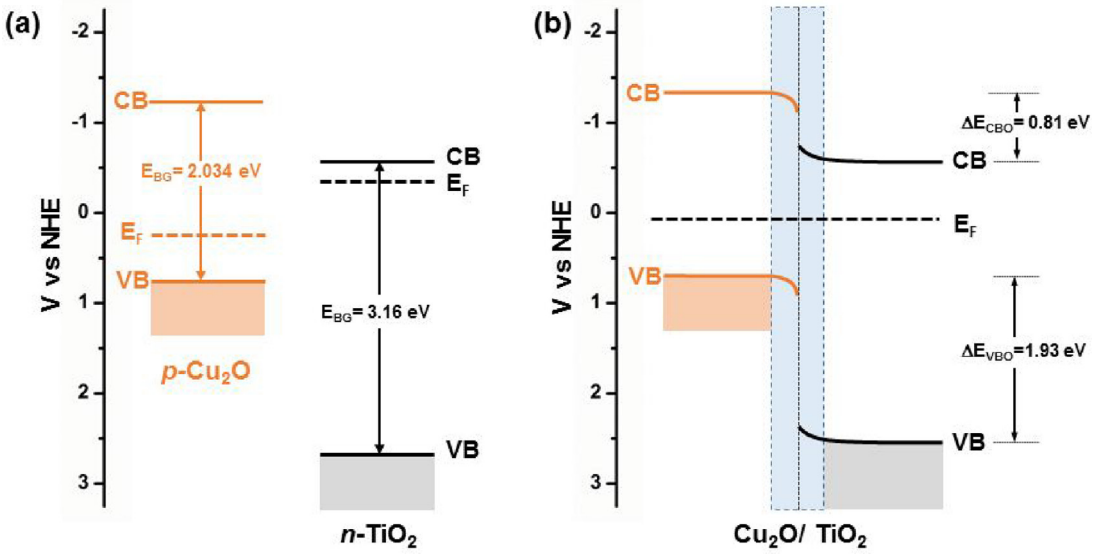

Fig. 5. Energy band diagrams for (a) Cu_2O and TiO_2 before contact and (b) Cu_2O/TiO_2 composite.

obtained for pure TiO_2 (Fig. S2). The deconvolution peaks of the O 1 s spectrum for the Cu_2O/TiO_2 requires a greater number of components than for Cu_2O and in particular, three curves centered in 530.01, 532.08 and 533.63 eV are necessary. The two last components could be assigned to hydroxyl groups and water molecules adsorbed on the TiO_2 surface [38,39]. It should be noticed that the hydroxylation and the presence of adsorbed water molecules benefits CO_2 photoreduction [20] (See Fig. S3, for details).

3.4. Optical properties and energy bands alignments at the heterojunction

Assessing the bands edge positions of Cu_2O and TiO_2 and the band alignment is important to understand the electron transfer process at the heterojunction and to determine the reactions that are thermodynamically feasible. The combined information from DRUV, UPS and XPS spectroscopies was used to determine electronic band alignments and the construction of the band energy diagram as discussed below.

DRUV spectra of Cu_2O, pure TiO_2, and Cu_2O/TiO_2 are shown in Fig. 4a. The absorption edges for pure Cu_2O and TiO_2 samples were approximately 600 and 390 nm, respectively. Analysis of Tauc plots indicates that the optical bandgaps are E_{BG} (Cu_2O) = 2.03 eV, (as a direct semiconductor) and E_{BG} (TiO_2) = 3.16 eV, (as an indirect semiconductor) [40] (Fig. S4). These figures agree with the previously reported values for Cu_2O [41] and TiO_2 [10].

Fig. 4b shows the UPS spectra of Cu_2O, TiO_2 and Cu_2O/TiO_2. By applying the method of linear approximation to the UPS spectra, the work function and the corresponding energy of the Fermi level of Cu_2O were estimated to be 4.70 and −4.70 eV, respectively. Similarly, the valence band maximum was calculated to be −5.20 eV. Considering the average bandgap energy value (2.03 eV for Cu_2O) obtained from the Tauc plots (Fig. S4, Supporting Information), the minimum of the conduction band is located at −3.17 eV. The quantities previously determined are referred to the vacuum level. Therefore, according to the relationship between the potential of the normal hydrogen electrode (NHE), $E^{\bullet}$, and the energy of the vacuum (E_{abs}), $E_{abs} = -E^{\bullet} - 4.44$ (at 298 K), the conduction and valence bands of Cu_2O are poised at −1.27 and 0.76 eV, respectively. Similarly, following this procedure for TiO_2, the estimated Fermi level (E_F), CB and VB vs NHE are −0.38, −0.57 and 2.59 eV, respectively (Fig. S5, Supporting Information).

After contact, the Fermi level of Cu_2O and TiO_2 equilibrates due to the formation of a *p-n* heterojunction at the interface of the

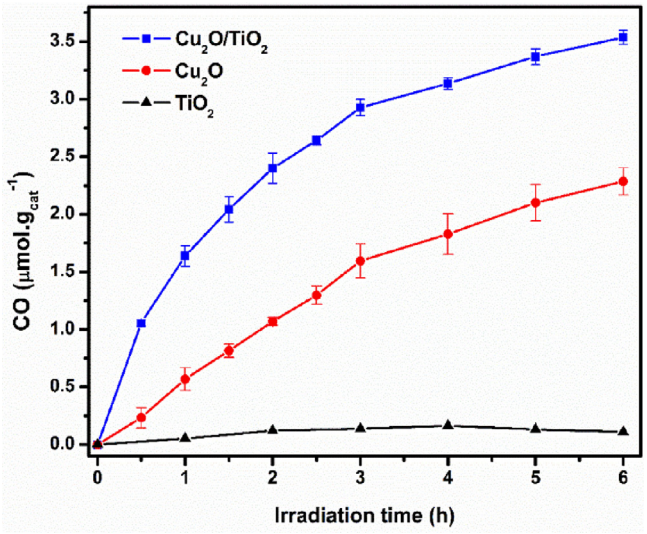

Fig. 6. Carbon monoxide evolution over Cu_2O/TiO_2 heterostructure (blue), Cu_2O (red) and TiO_2 (black) under UV-visible irradiation ($\lambda \geq 305$ nm). (For interpretation of the references to colour in this figure legend, the reader is referred to the web version of this article.)

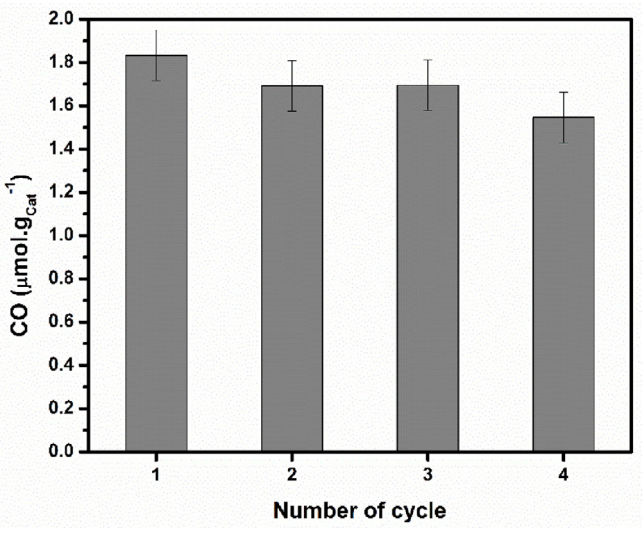

Fig. 7. Carbon monoxide production during 1 h-period in the recycling experiments (see text for details).

Cu_2O/TiO_2 composite [42]. This process alters the band positions, as observed by XPS. Fig. S5 in the Supporting Information provides the XPS spectra. The band alignment at the interface of Cu_2O/TiO_2 was determined following the method of Kraut [43]. To accurately determine the valence band offset, ΔE_{VBO}, the energy difference between the core level (E_{CL}) and the valence band maximum (E_{VBM}) in the pure materials, as well as the energy difference between the core levels at the interface of the heterostructure (ΔE_{CL}^{Int}) are needed. Eqs. (2) and (3) are used to calculate ΔE_{VBO} and ΔE_{CL}^{Int}, respectively:

$$\Delta E_{VBO} = \left(E_{CL}^{Cu_2O} - E_{VBM}^{Cu_2O}\right) - \left(E_{CL}^{TiO_2} - E_{VBM}^{TiO_2}\right) + \Delta E_{CL}^{Int} \quad (2)$$

$$\Delta E_{CL}^{Int} = \left(E_{CL}^{TiO_2} + E_{CL}^{Cu_2O}\right)^{Cu_2O/TiO_2} \quad (3)$$

The conduction band offset, ΔE_{CBO}, can be readily obtained from the bandgap energies (E_{BG}) of the pure materials and ΔE_{VBO}:

$$\Delta E_{CBO} = E_{BG}^{Cu_2O} - E_{BG}^{TiO_2} + \Delta E_{VBO} \quad (4)$$

Combining the information gathered during XPS and DRUV analyses reveals that for the nanocomposite $\Delta E_{VBO} = 1.93$ eV and $\Delta E_{CBO} = 0.81$ eV (Fig. 5). The energy difference between the conduction and valence bands for the materials in the composite are about 0.11 eV higher than the values before contact. From the previous observation and the onset value of the composite (Fig. 4b), the valence band maximum of Cu_2O in the composite is calculated to lie at 0.62 eV (vs NHE). The last figure is useful to calculate the apparent bandgap of Cu_2O in the composite, which together with ΔE_{VBO} and ΔE_{CBO} is needed to estimate the minimum of the conduction band of Cu_2O in the composite to be −1.39 eV (vs NHE) and the valence band maximum and conduction band minimum of TiO_2, which are depicted at 2.55 and −0.58 eV in Fig. 5, respectively [20].

Fig. 5 shows the energy diagram indicating the formation of a Type II (staggered) band heterostructure, whose highly energetic conduction band favors the reduction of CO_2 through photogenerated electrons. We assume that the assignment of the composite bands corresponds to values that are far from the Cu_2O/TiO_2 interface. Taking into account this observation, and considering that the energy differences between CB and E_F for TiO_2 as well as from VB and E_F for Cu_2O do not remain constant before and after contact, we showed in Fig. 5 the associated band bendings [44–46].

The energy difference between the valence band maximum of Cu_2O and the conduction band minimum of TiO_2 can be estimated as 1.33 and 1.2 eV for the separated semiconductors and the composite, respectively. This change indicates that under UV-visible irradiation, the electron transfer from the conduction band of TiO_2 to the valence band of Cu_2O (direct Z-scheme) could be favored due to the increased overlap of energy levels involved upon *p-n* heterojunction formation.

3.5. Photocatalytic CO_2 reduction

Irradiation of the composite with $\lambda \geq 305$ nm results in the selective formation of CO, (and O_2). The time series for CO evolution from the irradiated composite is shown in Fig. 6 together with the results obtained under similar conditions for pure Cu_2O and TiO_2. Control experiments for Cu_2O/TiO_2 showed that no CO evolved in the dark or when the irradiation was carried out in the absence of CO_2 under 1 atm argon (Fig. S6).

It is apparent from the results in Fig. 6 that the formation of the *p-n* heterojunction improves the CO_2 reduction efficiency. Considering the same initial stage of irradiation, the CO evolution rates were calculated to be 2.11 and 0.55 μmol g_{cat}^{-1} h^{-1} for Cu_2O/TiO_2 and Cu_2O, respectively, which represents a *ca.* 4-times enhancement for the composite. The ratio from the areas for the convolution of the irradiance of the lamp with the DRUV spectra of 1) Cu_2O/TiO_2 and 2) Cu_2O in the interval $305 \leq \lambda \leq 665$ nm indicates the nanocomposite absorbs *ca.* 2-times more photons than Cu_2O per unit mass under the experimental conditions in Fig. 6. Thus, only a 50% of the enhanced photocatalytic activity can be explained to arise from an increment in the oscillator strength (or the resulting increase of the integrated absorption per unit mass). Therefore, the synergistic effect from the materials in the nanocomposite is proposed to provide the remaining 50% photocatalytic enhancement.

The ratio of quantum efficiencies for CO production, Φ_{CO}, for Cu_2O/TiO_2 and Cu_2O can be easily calculated from the established relationships between the initial reaction rates ($R_{0,CO}$) and the absorbed photon fluxes I_a, which was established above,

$$\frac{\Phi_{CO}^{Cu_2O/TiO_2}}{\Phi_{CO}^{Cu_2O}} = \frac{R_{0,CO}^{Cu_2O/TiO_2}/I_a^{Cu_2O/TiO_2}}{R_{0,CO}^{Cu_2O}/I_a^{Cu_2O}} = \frac{R_{0,CO}^{Cu_2O/TiO_2}}{R_{0,CO}^{Cu_2O}} \times \frac{I_a^{Cu_2O}}{I_a^{Cu_2O/TiO_2}} = \frac{4}{1} \times \frac{1}{2} = 2 \quad (5)$$

Therefore, the relative quantum efficiencies in Eq. (5) clearly demonstrate that Cu_2O/TiO_2 has an enhanced photocatalytic activity over Cu_2O.

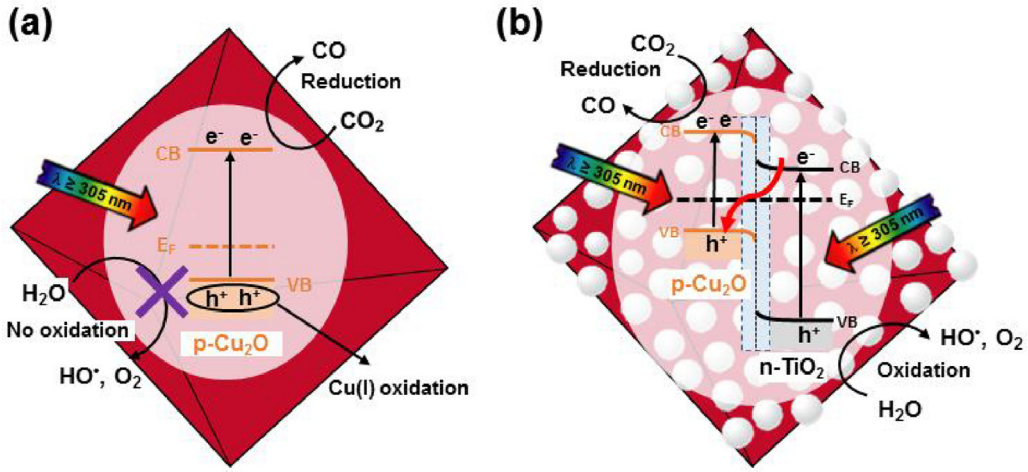

Scheme 2. Sketch of the proposed mechanism to account for CO_2 reduction induced by UV–vis irradiation ($\lambda \geq 305$ nm)) of (a) octahedral Cu_2O and (b) Cu_2O/TiO_2 composite.

Table 1
Summary of XPS analysis for Cu_2O and Cu_2O/TiO_2 photocatalysts at different irradiation times.

	Relative Components		Relative Components	
	Cu_2O		Cu_2O/TiO_2	
Irradiation time (h)	Cu(I)	Cu(II)	Cu(I)	Cu(II)
0	0.75	0.25	0.65	0.35
3	0.69	0.31	0.64	0.36
6	0.60	0.40	0.65	0.35

Another point of interest is that the evolution of CO decreases with the irradiation time. This is a characteristic of many photocatalytic processes [10] and, in particular, has been observed for the photocatalytic CO_2 reduction over α- Fe_2O_3/Cu_2O [20], and over pure Cu_2O and Cu_2O/RuOx systems [47]. The actual reason for this behavior is not well understood but possible causes for the non-linear time profile are commonly ascribed to the strong interaction between Cu_2O and CO, or the formation of O_2, which competes with carbon dioxide reduction [47]. To get more insight, we investigate the rate of CO evolution in repeated 1 h irradiation cycles. After each run, the reactor was thoroughly evacuated and re-loaded with the same amount of CO_2 and H_2O before irradiation. Fig. 7 shows that after 4 cycles, CO yields slightly diminish, in sharp contrast with the results obtained under continuous irradiation. These experiments indicate that the inhibition observed in Fig. 6 is not irreversible, and the catalyst may be recycled without significant loss of efficiency, if the products are periodically removed.

3.6. Analysis of the reaction mechanism

As discussed above, two different schemes commonly referred as (A) *double-charge transfer* and (B) *direct Z-scheme mechanisms* are often proposed to explain the electron transfer processes across the interface in *p-n* heterojunctions after the simultaneous excitation of the centers of Type II heterostructures [19,48]. To determine which of these two mechanisms is operative, the photocatalyst was separated from the reactor and analyzed by XPS after different photons doses to monitor the possible change in the copper oxidation state during the irradiation experiments. The most relevant results are summarized in Table 1, which details are provided in Fig. S7.

XPS and XRD analysis allow us to discard the possible photoreduction of Cu(I) [30,46] during the irradiation experiments for Cu_2O and Cu_2O/TiO_2 composite as no Cu(0) could be observed. On the other hand, as shown in Table 1, XPS analysis of pure Cu_2O shows a relative increment of the contribution of Cu(II) in the Cu $2p_{3/2}$ in relation to the Cu(I) content. Cu_2O photocorrosion might have been anticipated since Cu_2O irradiation generates a highly reductive conduction band electron, $E_{CB} = -1.27$ eV, but a valence band hole with insufficient energy to oxidize water [11] (Scheme 2a). This key point is also demonstrated during experiments presented below that have quantified the production of HO• radicals.

By contrast, in the Cu_2O/TiO_2 composite, the ratio Cu(II)/Cu(I) keeps constant along the entire photocatalytic reaction. To account for these results, we proposed that UV-visible irradiation induces the formation of an electron/hole pair in each photocatalytic center, Eq. (6):

$$Cu_2O/TiO_2 + h\nu_{(UV-visible)} \rightarrow Cu_2O\left(e^-_{CB}, h^+_{VB}\right)/TiO_2\left(e^-_{CB}, h^+_{VB}\right) \quad (6)$$

and after carrier generation, the electrons in the conduction band of TiO_2 are transferred to Cu_2O (see Scheme 2b):

$$Cu_2O\left(e^-_{CB}, h^+_{VB}\right)/TiO_2\left(e^-_{CB}, h^+_{VB}\right) \rightarrow Cu_2O\left(e^-_{CB}\right)/TiO_2\left(h^+_{VB}\right) + heat \quad (7)$$

and the TiO_2 holes localize on surface oxygen, forming $(Ti^{3+})_{latt}$ and $(Ti^{4+}O^{\bullet-})_{surf}$ paramagnetic species, respectively. By these processes, we achieved a heterostructure with strongly reductive electrons, $Cu_2O(e^-_{CB})$, and oxidative holes, $TiO_2(h^+_{VB})$, able to oxidize water. Water oxidation by TiO_2 is not only thermodynamically allowed but also kinetically feasible as revealed by EPR experiments, which indicate that surface trapped holes react with adsorbed molecules even at the extremely low temperatures used in the EPR studies [49].

$$TiO_2\left(h\nu_{VB}{}^+\right) + H_2O \rightarrow HO^\bullet + H^+ \quad (8)$$

The fluorescence spectra for the production of 7-hydroxycoumarin during irradiation of Cu_2O/TiO_2 is presented in Fig. S8 (Supplementary Information). The characteristic fluorescence peak at $\lambda_{em} = 456$ nm matches the reported spectrum of 7-hydroxycoumarin [28], which implies that only this species is produced [27]. Importantly, no peak for 7-hydroxycoumarin production was observed during 1) a dark control with Cu_2O/TiO_2, or 2) irradiated Cu_2O. These controls strongly support the assignment of HO•, an important intermediate for O_2 production, as a unique product from the photoactivity of the nanocomposite. The linear relationship between fluorescence intensity and irradiation time (Fig. S8) indicates a constant production rate for 7-hydroxycoumarin. Consequently, the production of HO• displayed in the inset of Fig. S8 (Supplementary Information) is

quantified by standard addition of 7-hydroxycoumarin to the samples. From the slope of the inset in Fig. S8 (Supplementary Information), the production rate of HO• is 0.22 (±0.03) μmol $g_{cat}^{-1}\,h^{-1}$. Comparatively, after 3 h of irradiation, the rate of production of CO is 5-times larger. By correcting the previous rates in a per photon basis using the stoichiometric consumptions of 2 e^-_{CB} and 1 h^+_{VB} for CO and HO• species produced, respectively, indicates that 40% of the theoretical amount of HO• is trapped by 7-hydroxycoumarin. The previous observation is not surprising for HO•, a high reactivity and short lived species with a lifetime $\tau \sim 1$ ns [28].

In the presence of CO_2, additional evidence of water oxidation by Cu_2O/TiO_2 nanostructures, comes from the analysis of the ratio between CO and O_2 yields. After 1 h of irradiation, we determined $CO/\mu mol\,g^{-1}{}_{cat} = 1.69 \pm 0.12$ and $O_2/\mu mol\,g^{-1}{}_{cat} = 0.83 \pm 0.06$, which gives $CO/O_2 = 1.69{:}0.83 = 2.03$, in close agreement with the expected reaction stoichiometry.

According to the Z-scheme, the anodic reaction takes place in the Cu_2O surface. In this regard, it is interesting to notice that the one electron homogeneous reduction potential for the monoelectronic reduction of CO_2 (Eq. (1)), is more negative than the conduction band level of Cu_2O ($E_{CB}(Cu_2O) = -1.39$ eV). Thus, in order to make the CO_2 reduction thermodynamically feasible, some stabilization must be invoked [50,51]. Alternatively, rapid hole scavenging by adsorbed molecular water could lead to electron accumulation in Cu_2O, and reduce CO_2 by a two-electron process,

$$2e^-_{CB,Cu_2O} + CO_2 + 2H^+ \rightarrow CO + H_2O \quad (9)$$

with lower energy demand ($E^{\bullet}(CO_2/CO) = -0.53$ V) [52], avoiding the formation of the high energy intermediate, $CO_2^{\bullet -}$. However, current evidence does not allow distinguishing between the two possibilities.

4. Conclusion

A Cu_2O/TiO_2 photocatalyst with high morphologic and crystallographic quality was synthetized by a simple solvothermal method. The new material shows a 4-times enhancement for the photoreduction rate of CO_2 induced by UV-visible irradiation in comparison to pure Cu_2O. Detailed analyses of the photocatalysts by XPS spectroscopy under operation, as well as the formation of HO• radicals in the Cu_2O/TiO_2 system, at variance with the results for pure Cu_2O, unequivocally prove a Z-scheme mechanism. The results obtained are of practical interest for photocatalysis and are also relevant for the understanding of photoinduced interfacial charge-transfer processes at the *p-n* heterojunction.

Acknowledgements

Research funding from the U.S. National Science Foundation under NSF CAREER award CHE-1255290 to M.I.G and from ANPCyT (Argentina) to M.A.G under project 1456 are gratefully acknowledged. R.Z thanks partial support from the University of Kentucky by a Research Challenge Trust Fund Fellowship. M.E.A thanks CONICET for a postdoctoral fellowship and ANPCyT for partially financing his stay at the University of Kentucky where this research was performed.

Appendix A. Supplementary data

Supplementary data associated with this article can be found, in the online version, at http://dx.doi.org/10.1016/j.apcatb.2017.05.058.

References

[1] Y. Izumi, Recent advances in the photocatalytic conversion of carbon dioxide to fuels with water and/or hydrogen using solar energy and beyond, Coord. Chem. Rev. 257 (2013) 171–186.
[2] X. Chang, T. Wang, J. Gong, CO_2 photo-reduction: insights into CO_2 activation and reaction on surfaces of photocatalysts, Energy Environ. Sci. 9 (2016) 2177–2196.
[3] S. Sato, T. Arai, T. Morikawa, Toward solar-driven photocatalytic CO_2 reduction using water as an electron donor, Inorg. Chem. 54 (2015) 5105–5113.
[4] G. Sahara, O. Ishitani, Efficient photocatalysts for CO_2 reduction, Inorg. Chem. 54 (2015) 5096–5104.
[5] E.E. Benson, C.P. Kubiak, A.J. Sathrum, J. Smieja, Electrocatalytic and homogeneous approaches to conversion of CO_2 to liquid fuels, Chem. Soc. Rev. 38 (2009) 89–99.
[6] (a) J. Schneider, H. Jia, J.T. Muckerman, E. Fujita, Thermodynamics and kinetics of CO_2, CO, and H^+ binding to the metal centre of CO_2 reduction, Chem. Soc. Rev. 41 (2012) 2036–2051;
(b) J. Agarwal, E. Fujita, H.F. Schaefer, J.T. Muckerman, Mechanisms for CO production from CO_2 using reduced rhenium tricarbonyl catalysts, J. Am. Chem. Soc. 134 (2012) 5180–5186;
(c) A.J. Morris, G.J. Meyer, E. Fujita, Molecular approaches to the photocatalytic reduction of carbon dioxide for solar fuels, Acc. Chem. Res. 42 (2009) 1983–1994.
[7] (a) H. Takeda, K. Koike, H. Inoue, O. Ishitani, Development of an efficient photocatalytic system for CO_2 reduction using rhenium(I) complexes based on mechanistic studies, J. Am. Chem. Soc. 130 (2008) 2023–2031;
(b) B. Gholamkhass, H. Mametsuka, K. Koike, T. Tanabe, M. Furue, O. Ishitani, Architecture of supramolecular metal complexes for photocatalytic CO_2 reduction: ruthenium-rhenium bi- and tetranuclear complexes, Inorg. Chem. 44 (2005) 2326–2336.
[8] A. Dhakshinamoorthy, S. Navalon, A. Corma, H. García, Photocatalytic CO_2 reduction by TiO_2 and releated titanium containing solids, Energy Environ. Sci. 5 (2012) 9217–9233.
[9] W. Fan, Q. Zhang, Y. Wang, Semiconductor-based nanocomposites for photocatalytic H_2 production and CO_2 conversion, Phys. Chem. Chem. Phys. 15 (2013) 2632–2649.
[10] S.N. Habisreutinger, L. Schmidt-Mende, J.K. Stolarczyk, Photocatalytic reduction of CO_2 on TiO_2 and other semiconductors, Angew. Chem. Int. Ed. 52 (2013) 2–39.
[11] P. Wardman, Reduction potentials of one-electron couples involving free radicals in aqueous solutions, J. Phys. Chem. Ref. Data 18 (1989) 1637–1755.
[12] S. Chen, T. Cao, Y. Gao, D. Li, F. Xiong, W. Huang, Probing surface structures of CeO_2 TiO_2, and Cu_2O nanocrystals with CO and CO_2 chemisorption, J. Phys. Chem. C 120 (2016) 21472–21485.
[13] I.K. Levy, M.A. Brusa, M.E. Aguirre, G. Custo, E. San Roman, M.I. Litter, M.A. Grela, Exploiting electron storage in TiO_2 nanoparticles for dark reduction of As(V) by accumulated electrons, Phys. Chem. Chem. Phys. 15 (2013) 10335–10338.
[14] R. Zhou, M.I. Guzman, CO_2 reduction under periodic illumination of ZnS, J. Phys. Chem. C 118 (2014) 11649–11656.
[15] P.E. de Jongh, J.J. Kelly, A catalyst for the photochemical decomposition of water? Chem. Comm. 12 (1999) 1069–1070.
[16] A. Paracchinol, V. Laporte, K. Sivula, M. Grätzel, E. Thimsen, Highly active oxide photocathode for photoelectrochemical water reduction, Nature Mater. 10 (2011) 456–461.
[17] Y. Wang, O. Wang, X. Zhan, F. Wang, M. Safdar, J. He, Visible light driven type II heterostructures and their enhanced photocatalysis properties: a review, Nanoscale 5 (2013) 83216–88339.
[18] H. Xu, S. Ouyang, L. Liu, D. Wang, T. Kako, J. Ye, Pourous-structured Cu_2O/TiO_2 nanojunction material toward efficient CO_2 photoreduction, Nanotechnology 16 (2014) 165402.
[19] L. Huang, F. Peng, H. Wang, H. Yu, Z. Li, Preparation and characterization of Cu_2O/TiO_2 nano?nano heterostructure photocatalysts, Catal. Comm. 10 (2009) 1839–1843.
[20] J.-C. Wang, L. Zhang, W.-X. Fang, J. Ren, Y.-Y. Li, H.-C. Yao, J.-S. Wang, Z.-J. Li, Enhanced photoreduction CO_2 activity over direct Z-scheme α-Fe_2O_3/Cu_2O heterostructures under visible light irradiation, ACS Appl. Mater. Interfaces 7 (2015) 8631–8639.
[21] K. Sekizawa, K. Maeda, K. Domen, K. Koike, O. Ishitani, Artificial Z-scheme constructed with a supramolecular metal complex and semiconductor for the photocatalytic reduction of CO_2, J. Am. Chem. Soc. 135 (2013) 4596–4599.
[22] K. Maeda, Z-scheme water splitting using two different semiconductor photocatalysts, ACS Catal. 3 (2013) 1486–1503.
[23] P. Zhou, J. Yu, M. Jaroniec, All-solid-state Z-scheme photocatalytic systems, Adv. Mater. 26 (2014) 4920–4935.
[24] D.-F. Zhang, H. Zhang, L. Guo, K. Zheng, X.-D. Han, Z. Zhang, Delicate control of crystallographic facet-oriented Cu_2O nanocrystals and the correlated adsorption ability, J. Mater. Chem. 19 (2009) 5220–5225.
[25] L. Liu, W. Yang, Q. Li, S. Gao, J.K. Shang, Synthesis of Cu_2O nanospheres decorated with TiO_2 nanoislands their enhanced photoactivity and stability under visible light illumination, and their post-illumination catalytic memory, ACS Appl. Mater. Interfaces 6 (2014) 5629–5639.

[26] A.J. Eugene, S.-S. Xia, M.I. Guzman, Aqueous photochemistry of glyoxylic acid, J. Phys. Chem. A 120 (2016) 3817–3826.
[27] Q. Xiang, J. Yu, P.K. Wong, Quantitative characterization of hydroxyl radicals produced by various photocatalysts, J. Colloid Interface Sci. 357 (2011) 163–167.
[28] G. Louit, S. Foley, J. Cabillic, H. Coffigny, F. Taran, A. Valleix, J.P. Renault, S. Pin, The reaction of coumarin with the OH radical revisited: hydroxylation product analysis determined by fluorescence and chromatography, Rad. Phys. Chem. 72 (2005) 119–124.
[29] L. Liu, W. Yang, Q. Li, K. Shang, Creation of $Cu_2O@TiO_2$ composite photocatalyst with *p-n* heterojunction formed on exposed Cu_2O facets their energy band alignment study, and their enhanced photocatalytic activity under illumination with visible light, ACS Appl. Mater. Interfaces 7 (2015) 1465–1476.
[30] L. Pan, J.-J. Zou, T. Zhang, S. Wang, Z. Li, L. Wang, X. Zhang, Cu_2O film via hydrothermal redox approach: morphology and photocatalytic performance, J. Phys. Chem. C 118 (2014) 16335–16343.
[31] Y. Xu, H. Wang, Y. Yu, L. Tian, W. Zhao, B. Zhang, Cu_2O Nanocrystal Surfactant-free room-temperature morphology-modulated synthesis and shape-dependent heterogenous organic catalytic activities, J. Phys. Chem. C 115 (2011) 15288–15296.
[32] G.-Z. Yuan, C.-F. Hsia, Z.-W. Lin, C. Chiang, Y.-W. Chiang, M.H. Huang, Highly facet-dependent photocatalytic properties of Cu_2O crystals established through the formation of Au-decorated Cu_2O heterostructures, Chem. Eur. J. 22 (2016) 12548–12556.
[33] K. Li, X. An, K.H. Park, M. Khraisheh, J. Tang, A critical review of CO_2 photo-conversion: catalysts and reactors, Catal. Today 224 (2014) 3–12.
[34] A.D. Handoko, J. Tang, Controllable proton and CO_2 photoreduction over Cu_2O with various morphologies, Int. J. Hydrogen Energy 38 (2013) 13017–13022.
[35] S. Poulston, P.M. Parlett, P. Stone, M. Bowker, Surface oxidation and reduction of CuO and Cu_2O studied using XPS and XAES, Surf. Interface Anal. 24 (1996) 811–820.
[36] I. Platzman, R. Brener, H. Haick, P. Tannenbaum, Oxidation of polycrystalline copper thin films at ambient conditions, J. Phys. Chem. C 112 (2008) 1101–1108.
[37] M. Logar, I. Bračko, A. Potočnik, B. Jančar, Cu and CuO/titanate nanobelt based network assemblies for enhanced visible light photocatalysis, Langmuir 30 (2014) 4852–4862.
[38] B. Erdem, R.A. Hunsicker, G.W. Simmons, E.D. Sudol, V.L. Dimonie, M. El-Aasser, XPS and FTIR surface characterization of TiO_2 particles used in polymer encapsulation, Langmuir 17 (2001) 2664–2669.
[39] A. Braun, F.A. Akgul, Q. Chen, S. Erat, T.-W. Huang, N. Jabeen, Z. Liu, B.S. Mun, S.S. Mao, X. Zhang, Observation of substrate orientation-dependent oxygen defect filling in thin $WO_{3-(}/TiO_2$ pulsed laser-deposited films with in situ XPS at high oxygen pressure and temperature, Chem. Mater. 24 (2012) 3473–3480.
[40] (a) Z. Li, S. Cong, Y. Xu, Brookite vs anatase TiO_2 in the photocatalytic activity for organic degradation in water, ACS Catal. 4 (2014) 3273–3280; (b) J. Buha, Solar absorption and microstructure of C-doped and H-co-doped TiO_2 thin films, J. Phys. D: Appl. Phys. 45 (2012) 385305.
[41] M. Yin, C.-K. Wu, Y. Lou, C. Burda, J.T. Koberstein, Y. Zhu, S. O'Brien, Copper oxide nanocrystals, J. Am. Chem. Soc. 127 (2005) 9506–9511.
[42] W. Lu, S. Gao, J. Wang, One-pot synthesis of Ag/ZnO self-assembled 3D hollow microspheres with enhanced photocatalytic performance, J. Phys. Chem. C 112 (2008) 16792–16800.
[43] E.A. Kraut, R.W. Grant, J.P. Waldrop, S.P. Kowalckyk, Precise determination of the valence-band edge in X-ray photoemission spectra: application to measurement of semiconductor interface potentials, Phys. Rev. Lett. 44 (1980) 1620–1623.
[44] B.L. Sharma, R.K. Purohit, Semiconductors Heterojunctions, first ed., Pergamon Press, Oxford- New York-Toronto-Sydney, 1974.
[45] A. Bera, S. Dey, A.J. Pal, Band mapping across a pn-junction in a nanorod by scanning tunneling microscopy, Nano Lett. 14 (2014) 2000–2005.
[46] S. Siol, J.C. Hellmann, S.D. Tilley, M. Grätzel, J. Morasch, J. Deuermeier, W. Jaegermann, A. Klein, ACS Appl. Mater. Interfaces 8 (2016) 21824–21831.
[47] E. Pastor, F.M. Pesci, A. Reynal, A.D. Handoko, M. Guo, X. An, A.J. Cowan, D.R. Klug, J.R. Durrant, J. Tang, Interfacial charge separation in Cu_2O/RuOx as a visible light driven CO_2 reduction catalyst, Phys. Chem. Chem. Phys. 16 (2014) 5922–5926.
[48] X. Wang, G. Liu, Z.-G. Chen, F. Li, L. Wang, G.Q. Lu, H.-M. Cheng, Enhanced photocatalytic hydrogen evolution by prolonging the lifetime of carriers in ZnO/CdS heterostructures, Chem. Comm. 345 (2009) 3452–3454.
[49] (a) T. Berger, M. Sterrer, O. Diwald, E. Knozinger, D. Panayotov, T.L. Thompson, J.T. yates jr., Light-Induced charge separation in anatase TiO_2 particles, J. Phys. Chem. B 109 (2005) 6061–6068;
(b) T. Berger, M. Sterrer, O. Diwald, E. Knozinger, Charge trapping and photoadsorption of O_2 on dehydroxylated TiO_2 nanocrystals?an electron paramagnetic resonance study, Chem. Phys. Chem. 6 (2005) 2104–2112;
(c) C.P. Kumar, N.O. Gopal, T.C. Wang, M.-S. Wong, S.C. Ke, EPR investigation of TiO_2 nanoparticles with temperature-dependent properties, J. Phys. Chem. B 110 (2006) 5223–5529;
(d) S.-C. Ke, T.-C. Wang, N.O. Wong, Low Temperature kinetics and energetics of the electron and hole traps in irradiated TiO_2 nanoparticles as revealed by EPR spectroscopy, J. Phys. Chem. B 110 (2006) 11628–11634.
[50] H.J. Freund, M.W. Roberts, Surface chemistry of carbon dioxide, Surf. Sci. Rep. 25 (1996) 225–273.
[51] V.P. Indrakanti, J.D. Kubicki, H.H. Schobert, Photoinduced activation of CO_2 on Ti-based heterogeneous catalysts: current state, chemical physics-based insights and outlook, Energy Environ. Sci. 2 (2009) 745–758.
[52] P.D. Tran, L.H. Wong, J. Barberbcd, J.S.C. Loo, Recent advances in hybrid photocatalysts for solar fuel production, Energy Environ. Sci. 5 (2012) 5902–5918.